

Solving the Einstein Constraints Numerically on Compact Three-Manifolds Using Hyperbolic Relaxation

Fan Zhang^{a,b} and Lee Lindblom^c

^a*Gravitational Wave and Cosmology Laboratory, Department of Astronomy, Beijing Normal University, Beijing 100875, China*

^b*Advanced Institute of Natural Sciences, Beijing Normal University at Zhuhai 519087, China and*

^c*Department of Physics, University of California at San Diego, La Jolla, CA 92093, USA*

(Dated: February 15, 2024)

The effectiveness of the hyperbolic relaxation method for solving the Einstein constraint equations numerically is studied here on a variety of compact orientable three-manifolds. Convergent numerical solutions are found using this method on manifolds admitting negative Ricci scalar curvature metrics, i.e. those from the H^3 and the $H^2 \times S^1$ geometrization classes. The method fails to produce solutions, however, on all the manifolds examined here admitting non-negative Ricci scalar curvatures, i.e. those from the S^3 , $S^2 \times S^1$, and the E^3 classes. This study also finds that the accuracy of the convergent solutions produced by hyperbolic relaxation can be increased significantly by performing fairly low-cost standard elliptic solves using the hyperbolic relaxation solutions as initial guesses.

PACS numbers:

I. INTRODUCTION

Hyperbolic relaxation was introduced by Rüter, et al. [1] as a method of solving elliptic partial differential equations numerically using a hyperbolic evolution code, without the need to develop a stand alone elliptic solver. The basic idea is to transform the elliptic equations into hyperbolic ones whose late time solutions approach the solutions to the original elliptic problem. As a simple example consider the elliptic equation

$$\tilde{\nabla}^a \tilde{\nabla}_a \psi = f(\psi, x^a), \quad (1)$$

where $\tilde{\nabla}_a \tilde{\nabla}^a$ is a covariant Laplace operator, and $f(\psi, x^a)$ is a function that may depend on the scalar field ψ and the spatial coordinates x^a . The hyperbolic relaxation method introduces a non-physical time coordinate, t , and transforms Eq. (1) into the damped wave equation:

$$-\partial_t^2 \psi - \kappa \partial_t \psi + \tilde{\nabla}^a \tilde{\nabla}_a \psi = f(\psi, x^a), \quad (2)$$

where κ is a damping parameter. It is easy to show that all the solutions to the homogeneous, $f(\psi, x^a) = 0$, version of Eq. (2) with $\kappa > 0$ (on a domain without boundary or using outgoing boundary conditions on a domain with boundary) drive $\partial_t \psi$ toward zero, see Appendix A. Thus ψ approaches a solution to the original homogeneous elliptic Eq. (1). More generally the hyperbolic relaxation method can be applied to the inhomogeneous Eq. (1) in cases where the solutions to Eq. (2) drive $\partial_t \psi$ toward zero. This method has been used successfully to solve the Einstein constraint equations numerically for black hole spacetimes [1, 2].

This paper explores the use of the hyperbolic relaxation method for solving the Einstein constraint equations on compact orientable three-manifolds. A few solutions to the Einstein constraints were found numerically on a variety of these compact manifolds using standard elliptic numerical methods in Ref. [3]. Those elliptic methods (e.g. using the ksp linear solver and

the snes non-linear solver from the PETSC software library [4]) were found to be very inefficient. This inefficiency severely limited the ability to find solutions on compact orientable manifolds having topologies that required complicated multicube structures to represent them [5, 6]. Hyperbolic relaxation transports constraint violations throughout the computational domain more efficiently than the diffusive processes used by many elliptic solvers. Our motivation for this study was to determine whether hyperbolic relaxation could be useful for overcoming those inefficiency problems when solving the Einstein constraint equations for initial data on compact orientable initial surfaces.

The particular form of the Einstein constraint equation used in this study has a simple form belonging to the class of elliptic equations in Eq. (1):

$$\tilde{\nabla}^a \tilde{\nabla}_a \psi = \frac{1}{8} \psi \left(\tilde{R} - \psi^4 \langle \tilde{R} \rangle \right), \quad (3)$$

where $\tilde{\nabla}_a$ is the covariant derivative and \tilde{R} the scalar curvature determined by a positive definite metric \tilde{g}_{ab} . The constant $\langle \tilde{R} \rangle$ is the spatial average of the scalar curvature,

$$\langle \tilde{R} \rangle = \frac{\int \sqrt{\det \tilde{g}} \tilde{R} d^3x}{\int \sqrt{\det \tilde{g}} d^3x}. \quad (4)$$

The physical meaning of ψ determined by Eq. (3) is the conformal factor needed to transform \tilde{g}_{ab} into the Einstein initial value constraint satisfying physical spatial metric g_{ab} ,

$$g_{ab} = \psi^4 \tilde{g}_{ab}, \quad (5)$$

in a vacuum spacetime with cosmological constant Λ on a spacelike surface with mean curvature K given by

$$K^2 = 3\Lambda - \frac{3}{2} \langle \tilde{R} \rangle, \quad (6)$$

see Ref.[3] for details. The conformal factor, ψ , determined by Eq. (3) also has the interesting mathematical property that it transforms \tilde{g}_{ab} into a metric g_{ab} whose scalar curvature R is constant:

$$R = \langle \tilde{R} \rangle. \quad (7)$$

Thus ψ is a solution to the Yamabe problem [7] that constructs a constant scalar curvature geometry on the manifold.

The numerical methods used in this study to solve the hyperbolic relaxation Eq. (2) are described in Sec. II. Numerical results of using these methods on a variety of compact orientable three-manifolds are described in Sec. III. An elliptic refinement method for improving the accuracy of the numerical solutions found by hyperbolic relaxation is described in Sec. IV. This elliptic refinement method performs a standard elliptic solve with fairly lax convergence criteria using the hyperbolic relaxation results as its initial guess. The successes and failures of the tests reported here are summarized and discussed in Sec. V.

II. SOLVING HYPERBOLIC RELAXATION EQUATIONS NUMERICALLY

Numerical solutions to the hyperbolic relaxation version of the Einstein constraint Eq. (3) are studied here on a collection of compact orientable three-manifolds. These manifolds are represented as multicube structures [5], consisting of a collection of cubic regions \mathcal{B}_A whose faces $\partial_\alpha \mathcal{B}_A$ are identified with its neighbors' faces $\partial_\beta \mathcal{B}_B$ by a collection of maps $\Psi_{B\beta}^{A\alpha}$. The particular way the cubic regions are glued together by these maps determines the topologies of the manifolds represented in this way.

The differentiable structures of multicube manifolds are determined by a reference metric \tilde{g}_{ij} that (together with the maps $\Psi_{B\beta}^{A\alpha}$) determines the continuity of vector and tensor fields across the interface boundaries between regions. In particular these reference metrics can be used to construct the outward directed unit normal vectors \tilde{n}^i at each point on each face of each cubic region. The differentiable structure ensures the outward directed unit normals are identified with the corresponding inward directed normals on the adjoining faces of neighboring regions. The C^1 reference metrics for the manifolds included in this study were constructed as described in Ref. [8]. The collection of Cartesian coordinate charts in the cubic regions of the multicube structure, including its boundary identification maps $\Psi_{B\beta}^{A\alpha}$ and the differential structure provided by the reference metric \tilde{g}_{ij} , serves as a global atlas of coordinate charts for these manifolds. These reference metrics are also used as the conformal metrics in the solutions to the Einstein constraint equations studied here.

The hyperbolic relaxation version of the Einstein con-

straint Eq. (3) is given by

$$-\partial_t^2 \psi - \kappa \partial_t \psi + \tilde{\nabla}^a \tilde{\nabla}_a \psi = \frac{1}{8} \psi \left(\tilde{R} - \psi^4 \langle \tilde{R} \rangle \right). \quad (8)$$

This equation is solved numerically by converting it into the first-order symmetric hyperbolic system,¹

$$\partial_t \psi = -\Pi, \quad (9)$$

$$\partial_t \Pi + \tilde{g}^{ij} \tilde{\nabla}_i \Phi_j = -\kappa \Pi + \frac{1}{8} \psi \left(\tilde{R} - \psi^4 \langle \tilde{R} \rangle \right), \quad (10)$$

$$\partial_t \Phi_i + \tilde{\nabla}_i \Pi = \gamma_2 \left(\tilde{\nabla}_i \psi - \Phi_i \right). \quad (11)$$

The auxiliary first-order field Π is equivalent to $-\partial_t \psi$ from Eq. (9), while Φ_i is equivalent to $\tilde{\nabla}_i \psi$ when the constraint $\mathcal{C}_i \equiv \Phi_i - \tilde{\nabla}_i \psi = 0$ is satisfied. The constant $\gamma_2 > 0$ ensures that Eq. (11) damps away any constraint violations that may be introduced during the evolution. This first-order symmetric hyperbolic representation of the hyperbolic relaxation equation has the same principal parts, and therefore the same characteristic fields, as the system introduced in Ref. [9]. The propagating characteristic fields U^\pm with characteristic speeds ± 1 are given by

$$U^\pm = \Pi \pm \tilde{n}^i \Phi_i - \gamma_2 \psi, \quad (12)$$

where \tilde{n}^i is the outward directed unit normal vector at the boundary. As in any first-order symmetric hyperbolic system, boundary conditions are imposed on the incoming characteristic fields (U^- in this case) at each boundary point of each cubic region. At the interface boundaries between cubic regions these incoming fields are set to the values of the outgoing fields (U^+ in this case) copied from the corresponding boundary points of the neighboring region.

III. NUMERICAL RESULTS

Numerical solutions to the hyperbolic relaxation version of the Einstein constraint Eq. (8) have been computed in this study for a collection of ten compact orientable three-manifolds. These manifolds, listed in Table I, represent examples from five of the eight Thurston geometrization classes. The manifold names used here are those from Ref. [8], which includes the multicube structures of each manifold and explains in detail how the reference metrics, \tilde{g}_{ij} , are constructed. Table I also lists the spatial average of the Ricci curvature $\langle \tilde{R} \rangle$, defined in Eq. (4), the spatial volume $\tilde{\mathcal{V}}$, defined by

$$\tilde{\mathcal{V}} = \int \sqrt{\det \tilde{g}} d^3 x, \quad (13)$$

¹ Rüter, et al. [1] use a slightly different first-order representation of the Einstein constraints, see Eqs. (17)–(19) of their paper.

TABLE I: Compact orientable three-manifolds used in this study to test the hyperbolic relaxation method for solving the Einstein constraint equations.

Manifold	$\langle \tilde{R} \rangle$	\tilde{V}	Geometrization Class
$G2 \times S1$	-2.9676	15.287	$H^2 \times S^1$
$G5 \times S1$	-2.9676	61.149	$H^2 \times S^1$
Seifert-Weber Space	-4.7990	27.327	H^3
Sixth-Turn Space (E5)	0.0028	11.126	E^3
$KB/n2 \times \sim S1$	1.2715	48.946	E^3
$SFS[RP2.n2 : (2, 1)(2, -1)]$	1.2715	48.946	E^3
$S2 \times S1$	2.6878	16.768	$S^2 \times S^1$
$S3$	5.8899	36.592	S^3
$L(10, 3)$	1.7134	28.029	S^3
$SFS[S2 : (2, 1)(2, 1)(2, -1)]$	2.6552	19.150	S^3

and the Thurston geometrization class for each manifold.

The hyperbolic relaxation Eqs. (9)–(11) were solved using the multicube coordinate systems described in Ref. [6] for these manifolds. These representations consist of Cartesian coordinate charts within a collection of non-overlapping cubic regions that intersect only at the interfaces between neighboring cubes. The hyperbolic relaxation equations were solved using pseudo-spectral methods on Gauss-Lobatto collocation points in each cubic region. The time evolutions were performed using an eighth-order Dormand-Prince integrator with the error tolerance set to 10^{-12} . Boundary conditions were imposed at the interfaces between cubic regions using the multi-penalty method.

The Einstein constraint damping parameter, κ , that appears in Eq. (8), was set in these tests to the value,

$$\kappa = \frac{2\pi}{\tilde{V}^{1/3}}, \quad (14)$$

where $\tilde{V}^{1/3}$ represents a characteristic length scale of the manifold. The first-order scalar-wave constraint damping parameter, γ_2 , was set to the relatively large value $\gamma_2 = 100$ in these tests to ensure that violations of the scalar-wave constraint, $\mathcal{C} = \Phi_i - \tilde{\nabla}_i \psi$, were strongly suppressed.

Figure 1 shows the time dependence of $\|\partial_t \psi\|$, the L_2 norm of $\partial_t \psi$, defined by

$$\|\partial_t \psi\|^2 = \frac{1}{\tilde{V}} \int (\partial_t \psi)^2 \sqrt{\det \tilde{g}} d^3 x, \quad (15)$$

for the numerical evolutions of Eqs. (9)–(11) on each of the manifolds listed in Table I. The solid (black) curves represent the evolutions on the $G2 \times S1$, $G5 \times S1$ and the Seifert-Weber manifolds. Those evolutions reduce $\|\partial_t \psi\|$ to small values at late times, so hyperbolic relaxation is successful in computing approximate solutions to the Einstein constraint equation at late times for those cases. The evolutions shown as dashed (red) or dotted (blue) curves represent the evolutions on the remaining manifolds in this study. Those evolutions show $\|\partial_t \psi\|$ growing

exponentially (or faster), thus hyperbolic relaxation fails to produce solutions to the Einstein constraint equation in those cases. Appendix A provides an analysis of the stability of these hyperbolic relaxation evolutions. That analysis shows that hyperbolic relaxation evolutions are likely to be stable on compact manifolds with $\langle \tilde{R} \rangle \leq 0$, and unstable on those manifolds with $\langle \tilde{R} \rangle > 0$, which is consistent with these numerical results.

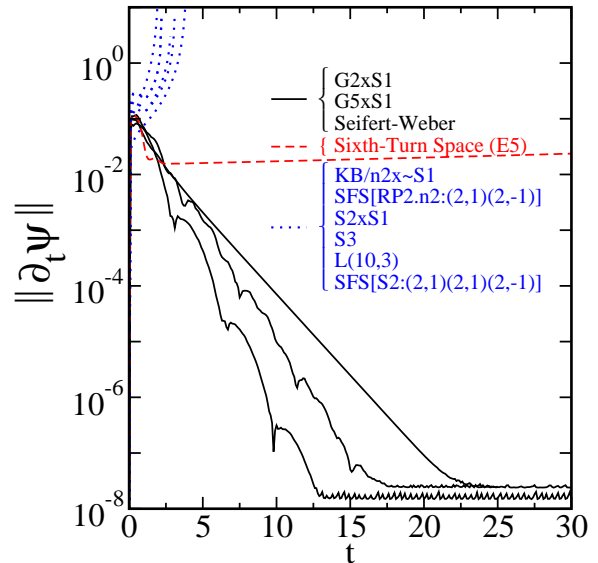


FIG. 1: . The norm $\|\partial_t \psi\|$ evolves toward zero for the $G2 \times S1$, $G5 \times S1$, and the Seifert-Weber manifolds, indicating that hyperbolic relaxation successfully solves the Einstein constraints asymptotically on these manifolds. However, $\|\partial_t \psi\|$ grows without bound on the other manifolds studied here, so hyperbolic relaxation fails to find solutions to the Einstein constraints on those manifolds.

The evolutions shown in Fig. 1 were computed at the same numerical resolution for each manifold: $N = 35$ grid points in each dimension in each cube of the multicube structure. Figure 2 illustrates $\|\partial_t \psi\|$ for the evolutions on the Seifert-Weber manifold using a sequence of numerical resolutions in the range $16 \leq N \leq 56$. These results demonstrate that $\|\partial_t \psi\|$ converges toward zero at late times as the resolution N is increased. The results for evolutions on the $G2 \times S1$ and the $G5 \times S1$ manifolds have similar late time convergences, so those graphs are not included here.

The Hamiltonian constraint \mathcal{H} for the initial value problem described in Eq. (3) can be written in its original geometric form:

$$\mathcal{H} = R - \langle \tilde{R} \rangle, \quad (16)$$

where R is the Ricci scalar curvature computed from the physical metric g_{ij} defined in Eq. (5). The constraint norm $\|\mathcal{H}\|$ defined by

$$\|\mathcal{H}\|^2 = \frac{1}{\tilde{V}} \int \mathcal{H}^2 \sqrt{\det \tilde{g}} d^3 x, \quad (17)$$

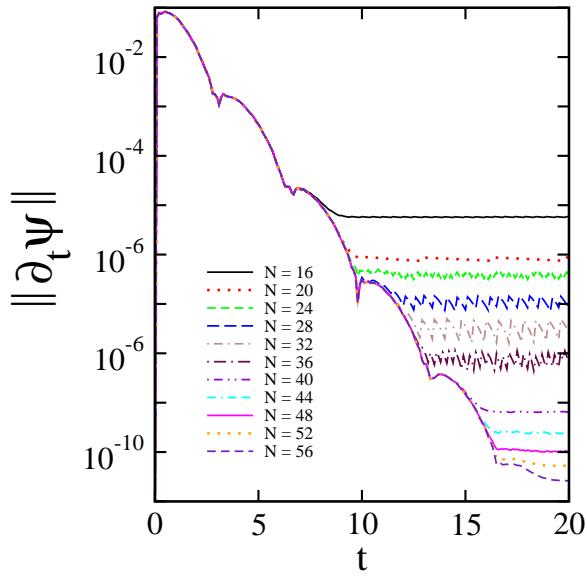


FIG. 2: . The evolutions of the norm $\|\partial_t \psi\|$ at different spatial resolutions, $16 \leq N \leq 56$, for hyperbolic relaxation evolutions on the Seifert-Weber manifold. The late time convergence of $\|\partial_t \psi\|$ toward zero as N is increased demonstrates that hyperbolic relaxation does produce numerically convergent solutions to the Einstein constraint equation for this case.

is a quantitative measure of how well the original Einstein constraints are satisfied. Figures 3, 4, and 5 illustrate the time dependence of $\|\mathcal{H}\|$ for the hyperbolic relaxation evolutions on the $G2 \times S1$, $G5 \times S1$, and Seifert-Weber manifolds respectively using a range of numerical resolutions $16 \leq N \leq 56$.

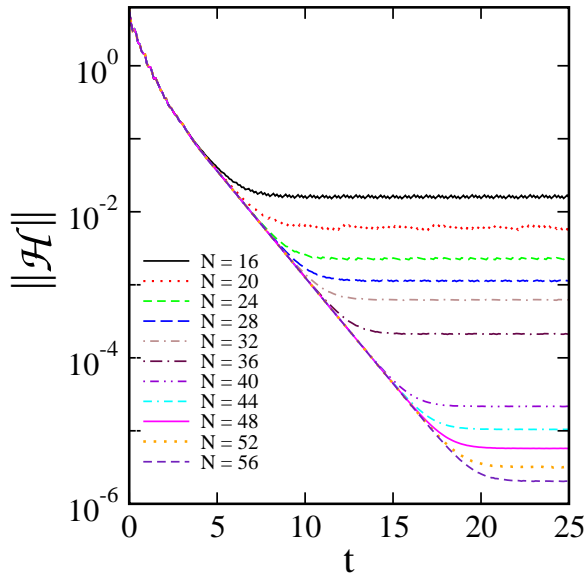


FIG. 3: . The Hamiltonian constraint norm $\|\mathcal{H}\|$ as a function of time, t , for hyperbolic relaxation evolutions on the $G2 \times S1$ manifold.

Each of the evolutions in Figs. 3, 4, and 5 show the

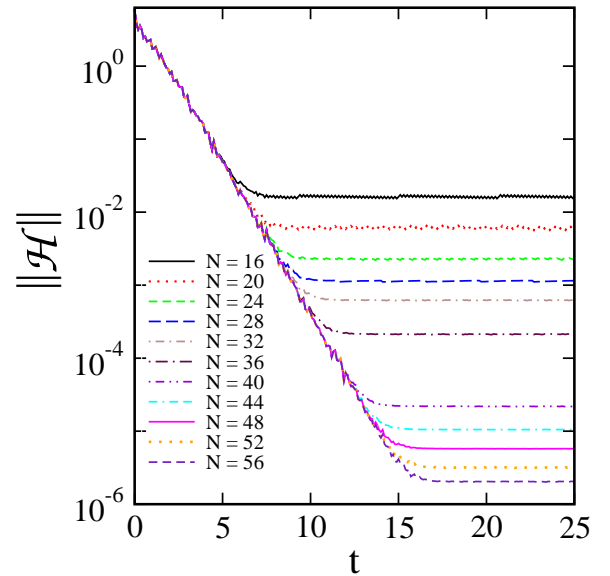


FIG. 4: . The Hamiltonian constraint norm $\|\mathcal{H}\|$ as a function of time, t , for hyperbolic relaxation evolutions on the $G5 \times S1$ manifold.

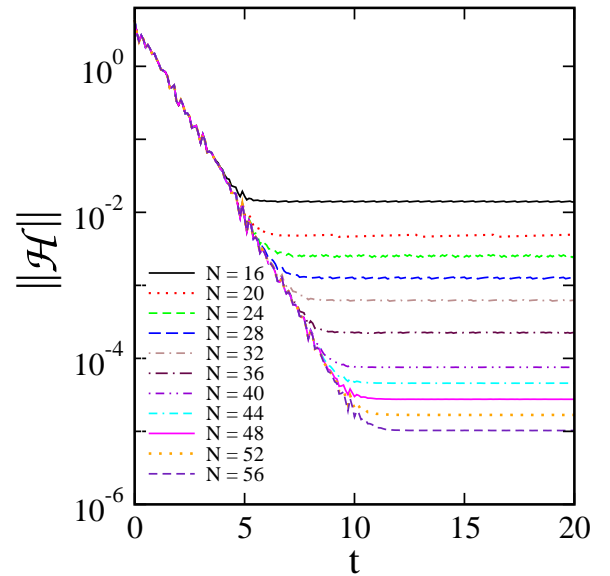


FIG. 5: . The Hamiltonian constraint norm $\|\mathcal{H}\|$ as a function of time, t , for hyperbolic relaxation evolutions on the Seifert-Weber manifold.

Hamiltonian constraint norm $\|\mathcal{H}\|$ initially decreasing (approximately) exponentially, and then becoming (essentially) time independent at late times. The late time asymptotic values of $\|\mathcal{H}\|$ have been extracted from these evolutions at the time $t = 25$ for the evolutions on the $G2 \times S1$ and $G5 \times S1$ manifolds, and at the time $t = 20$ for the Seifert-Weber manifold. These late time Hamiltonian constraint norms have been plotted as the solid (black) curves in Figs. 6, 7, and 8 as functions of the spatial resolution N . These results show that hyperbolic relax-

ation does produce numerically convergent solutions to the Einstein constraint equation on the $G2 \times S1$, $G5 \times S1$ and the Seifert-Weber manifolds.

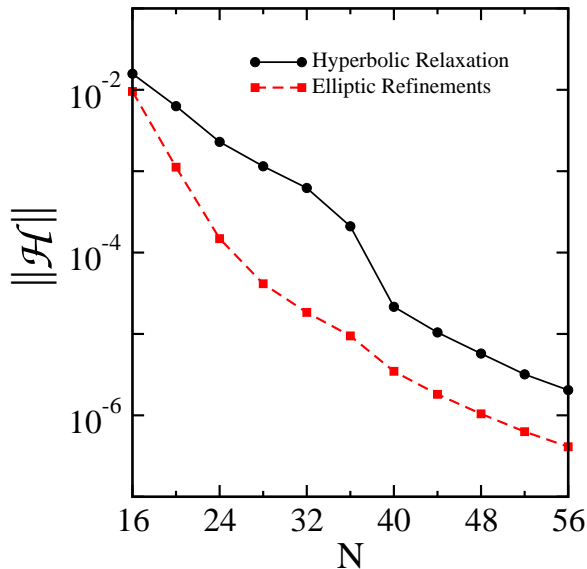


FIG. 6: The Hamiltonian constraint norm $\|\mathcal{H}\|$ as a function of the spatial resolution N on the $G2 \times S1$ manifold. The results from hyperbolic relaxation evolutions (evaluated at the time $t = 25$) are represented as the solid (black) curve and the elliptic refinements of these results are represented as the dashed (red) curve.

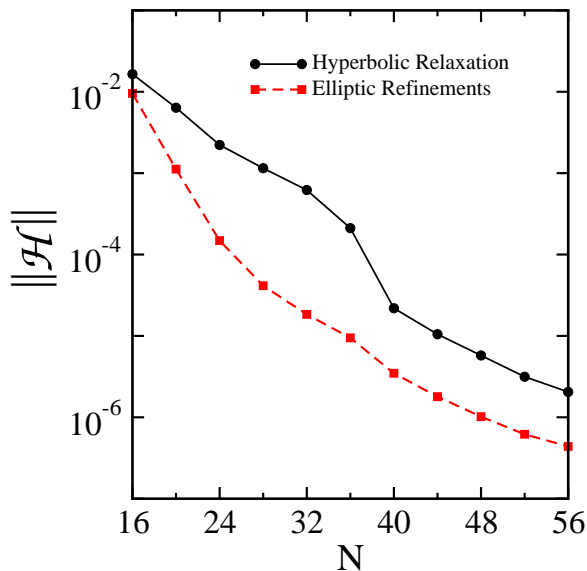


FIG. 7: The Hamiltonian constraint norm $\|\mathcal{H}\|$ as a function of the spatial resolution N on the $G5 \times S1$ manifold. The results from hyperbolic relaxation evolutions (evaluated at the time $t = 25$) are represented as the solid (black) curve and the elliptic refinements of these results are represented as the dashed (red) curve.

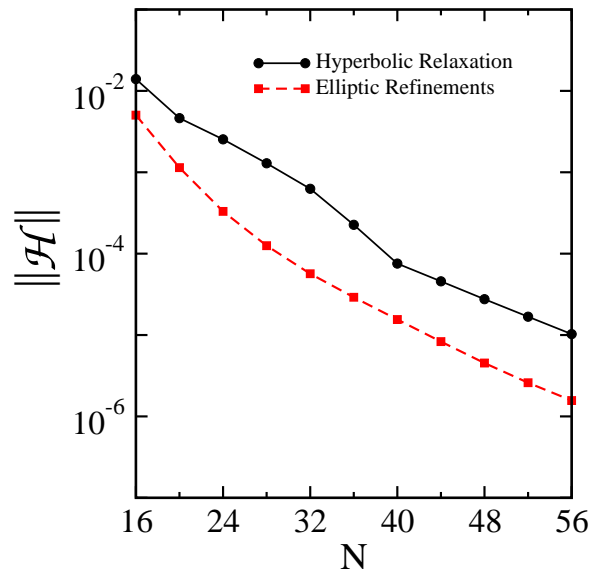


FIG. 8: The Hamiltonian constraint norm $\|\mathcal{H}\|$ as a function of the spatial resolution N on the Seifert-Weber manifold. The results from hyperbolic relaxation evolutions (evaluated at the time $t = 20$) are represented as the solid (black) curve and the elliptic refinements of these results are represented as the dashed (red) curve.

IV. ELLIPTIC REFINEMENTS

The hyperbolic relaxation evolutions of the Einstein constraint equation illustrated in Figs. 3–5 show that the Hamiltonian constraint norms $\|\mathcal{H}\|$ approach resolution dependent constant values at late times. What determines these late time values of $\|\mathcal{H}\|$ in these evolutions? Are these simply determined by the truncation errors in the numerical representations of the conformal factor ψ ? Or, is some other numerical effect setting a higher error floor for the values of the late time constraint norms? In an effort to understand these questions we performed standard numerical elliptic solves (using the ksp linear solver and the snes non-linear solver from the PETSC software library) using the final hyperbolic relaxation results as initial guesses. The error tolerance parameters for these elliptic solves were set at fairly large values to keep the cpu run times reasonably short. The resulting values of the Hamiltonian constraint norms $\|\mathcal{H}\|$ for these elliptic refinement computations are shown as the dashed (red) curves in Figs. 6–8. The resulting $\|\mathcal{H}\|$ from the elliptic refinement computations are about an order of magnitude smaller than those from the hyperbolic relaxation evolutions. This means that numerical truncation error is not the limiting factor in the accuracy of the hyperbolic relaxation evolutions.

While we do not fully understand why elliptic refinement is able to improve the hyperbolic relaxation results so significantly. However, the graphs of $\|\partial_t \psi\|$ in Fig. 2 might provide some insight. Our numerical implementation of the hyperbolic relaxation equations does not

drive $||\partial_t\psi||$ to zero, or even to double precision roundoff levels. This means that the hyperbolic relaxation evolutions of the conformal factor ψ never get to completely time independent states. The oscillations in $||\partial_t\psi||$ seen in some of the resolutions in Fig. 2 suggest that the second time derivatives $\partial_t^2\psi$ may be even larger than $\partial_t\psi$ in some cases. The fact that $\partial_t\psi$ and $\partial_t^2\psi$ do not vanish in the late time numerical hyperbolic evolutions provides one mechanism that could prevent the Hamiltonian constraint norm $||\mathcal{H}||$ from reaching truncation error levels.

We attempted to find a way to suppress the anomalous time dependence at late times in our numerical solutions to the hyperbolic relaxation equation (e.g. by adjusting the damping coefficient κ , reducing the timestep error tolerance, increasing the scalar-wave constraint damping coefficient γ_2 , etc.). But we were not successful in improving the results reported here. These results suggest that the accuracy of the hyperbolic relaxation method could be improved significantly if a way could be found to drive $\partial_t\psi$ and $\partial_t^2\psi$ more effectively to smaller levels at late times. Alternatively, using elliptic refinement can be used to improve the accuracy of those solutions significantly at relatively low additional computational cost.

V. DISCUSSION

This study explores the use of hyperbolic relaxation to solve the Einstein constraint equations numerically on compact orientable three-manifolds. A primary result of this study is that hyperbolic relaxation evolutions of the Einstein constraints are unstable on manifolds with positive conformal scalar curvature averages, $\langle\tilde{R}\rangle > 0$, while those with negative curvatures, $\langle\tilde{R}\rangle < 0$, are stable. This result severely limits the class of manifolds on which hyperbolic relaxation can be used successfully.

A second important result of this study is that our implementation of the hyperbolic relaxation method does not produce solutions whose accuracy is limited by truncation error. The late time errors in $\partial_t\psi$ and \mathcal{H} are dominated by their values along the edges and at a few collocation points near the edges of the cubic coordinate patches. These maximum errors converge to zero with increasing numerical resolution in much the same way as the L_2 norms shown in the figures. Our attempts to reduce these errors further by adjusting the filtering and the various damping parameters were not successful. The fact that these errors do not converge all the way to truncation error levels shows, however, that our code's implementation of the hyperbolic boundary conditions along those edges is not optimal.

Finally, a third important result of this study is the fact that the accuracy of the hyperbolic relaxation solutions can be improved by about an order of magnitude by doing a fairly low cost standard elliptic solve using the hyperbolic relaxation results as initial guesses. The elliptic solver imposes a different set of boundary conditions in a different way than the hyperbolic evolution system.

These results show that the elliptic solver does a better job than the hyperbolic evolution code of implementing the correct physical boundary conditions.

Appendix A

This appendix analyzes the stability of the hyperbolic relaxation method for finding solutions to the Einstein constraint equations. Let ψ_0 denote a solution to the Einstein constraints given in Eq. (3),

$$\tilde{\nabla}^a\tilde{\nabla}_a\psi_0 = \frac{1}{8}\psi_0\left(\tilde{R} - \psi_0^4\langle\tilde{R}\rangle\right). \quad (\text{A1})$$

We examine the stability of hyperbolic relaxation evolutions by defining $\delta\psi = \psi - \psi_0$ and studying the solutions to the linearized hyperbolic relaxation Eq. (8):

$$-\partial_t^2\delta\psi - \kappa\partial_t\delta\psi + \tilde{\nabla}^a\tilde{\nabla}_a\delta\psi = \frac{1}{8}\delta\psi\left(\tilde{R} - 5\psi_0^4\langle\tilde{R}\rangle\right). \quad (\text{A2})$$

Multiplying this equation by $\partial_t\delta\psi$ and integrating over a compact manifold (such as those included in this study) results in the equation

$$\frac{dE}{dt} = -2\int\kappa(\partial_t\delta\psi)^2\sqrt{\det\tilde{g}}d^3x, \quad (\text{A3})$$

where E is a perturbation energy defined by

$$E = \int\left[(\partial_t\delta\psi)^2 + \tilde{\nabla}^a\delta\psi\tilde{\nabla}_a\delta\psi + \frac{1}{8}(\delta\psi)^2\left(\tilde{R} - 5\psi_0^4\langle\tilde{R}\rangle\right)\right]\sqrt{\det\tilde{g}}d^3x. \quad (\text{A4})$$

Equation (A3) shows that all near-equilibrium evolutions of the hyperbolic relaxation equation drive the perturbation energy E to smaller values. The kinetic terms on the first line of the left side of Eq. (A4) are positive definite, while the potential-like terms on the second line do not have definite sign.

If the potential-like terms in Eq. (A4) are non-negative, then E would be positive definite, including for example the homogeneous case where the right side of Eq. (A2) vanishes. In this case hyperbolic relaxation produces stable evolutions that drive E towards its minimum value. However, if the potential-like terms are negative, then E would not be bounded below, and unstable evolutions would occur. We note that \tilde{R} and $\langle\tilde{R}\rangle$ are related on compact orientable manifolds by the identities

$$\int\tilde{R}\sqrt{\det\tilde{g}}d^3x = \int\langle\tilde{R}\rangle\sqrt{\det\tilde{g}}d^3x, \quad (\text{A5})$$

$$\int\psi_0\tilde{R}\sqrt{\det\tilde{g}}d^3x = \int\psi_0^5\langle\tilde{R}\rangle\sqrt{\det\tilde{g}}d^3x. \quad (\text{A6})$$

The first identity is just the definition of $\langle\tilde{R}\rangle$ from Eq. (4), while the second is obtained by integrating

Eq. (A1) over the manifold. These identities suggest that the following approximate equality should also be true,

$$\int \tilde{R} \sqrt{\det \tilde{g}} d^3x \approx \int \psi_0^4 \langle \tilde{R} \rangle \sqrt{\det \tilde{g}} d^3x. \quad (\text{A7})$$

For manifolds with reference metrics having positive average scalar curvatures, $\langle \tilde{R} \rangle > 0$, the term proportional to $\langle \tilde{R} \rangle$ in E is negative definite. Compared to Eq. (A7), the additional factor of 5 multiplying the $\langle \tilde{R} \rangle$ term in E , should make that term dominate over the term containing \tilde{R} in most (if not all) cases. In these cases E will not be bounded below and the hyperbolic relaxation evolutions will be unstable. Conversely for manifolds where $\langle \tilde{R} \rangle < 0$, the term proportional to $\langle \tilde{R} \rangle$ in E is positive definite, and hyperbolic relaxation is likely to be stable. This analysis of the stability of the hyperbolic relaxation method is only qualitative. However, the results of the numerical tests reported in Sec. III show that in practice

the sign of $\langle \tilde{R} \rangle$ is a useful predictor of the stability or instability of this method, as suggested by this analysis.

Acknowledgments

We thank Nicholas Taylor for a number of helpful discussions about the numerical methods used in this study, and David Hilditch and Hannes Rüter for their comments on an earlier draft of this paper. L.L. thanks the Department of Physics, National Central University, Zhongli, Taiwan for their hospitality during a visit in which a portion of this research was completed. F.Z. was supported in part by the National Natural Science Foundation of China grants 12073005 and 12021003. L.L. was supported in part by the National Science Foundation grant 2012857 to the University of California at San Diego, USA.

-
- [1] H. R. Rüter, D. Hilditch, M. Bugner, and B. Brugmann, *Phys. Rev. D* **98**, 084044 (2018).
 - [2] T. Assumpcao, L. R. Werneck, T. Pierre-Jacques, and Z. B. Etienne, *Phys. Rev. D* **105**, 104037 (2022).
 - [3] F. Zhang and L. Lindblom, *Gen. Relativ. Gravit.* **54**, 131 (2022).
 - [4] S. Balay, S. Abhyankar, M. F. Adams, S. Benson, J. Brown, P. Brune, K. Buschelman, E. Constantinescu, L. Dalcin, A. Dener, et al., *Tech. Rep. ANL-21/39 - Revision 3.16*, Argonne National Laboratory (2021).
 - [5] L. Lindblom and B. Szilágyi, *J. Comput. Phys.* **243**, 151 (2013).
 - [6] L. Lindblom, O. Rinne, and N. W. Taylor, *J. Comput. Phys.* **410**, 110957 (2022).
 - [7] H. Yamabe, *Osaka J. Math.* **12**, 21 (1960).
 - [8] L. Lindblom, N. W. Taylor, and O. Rinne, *J. Comput. Phys.* **313**, 31 (2016).
 - [9] M. Holst, L. Lindblom, R. Owen, H. P. Pfeiffer, M. A. Scheel, and L. E. Kidder, *Phys. Rev. D* **70**, 084017 (2004).